International Journal of Heat and Mass Transfer 64 (2013) 361–374

Contents lists available at SciVerse ScienceDirect

International Journal of Heat and Mass Transfer

journal homepage: www.elsevier.com/locate/ijhmt

Numerical analysis of electric force influence on heat transfer in a channel flow (theory based on saturated porous medium approach) ☆

Suwimon Saneewong Na Ayuttaya, Chainarong Chaktranond *, Phadungsak Rattanadecho

Department of Mechanical Engineering, Faculty of Engineering, Thammasat University (Rangsit Campus), Khlong Luang, Pathum Thani 12120, Thailand

ARTICLE INFO

Article history:
Received 4 October 2012
Received in revised form 3 April 2013
Accepted 6 April 2013

Keywords:
Electrohydrodynamic (EHD)
Heat transfer
Saturated porous medium
Shear flow

ABSTRACT

The present paper reports the influence of electrode and ground arrangement on electrically-driven airflow and heat transfer enhancement in a saturated porous medium placed in a channel flow. In simulations, the inlet velocity and temperature of air entering a test section are controlled at 0.35 m/s and 60 °C, respectively. High electrical voltage is tested in the range of 0–30 kV. The numerical results show+ that when electric field is applied, swirling flow caused by shear flow effect is observed. When electrode is placed near ground, swirling flow is small but it has a high strength. In addition, the strength of swirling flow is increased by increasing electrical voltage. With occurrence of swirling flow, the heat transfer is totally higher than the case of conventional hot-airflow. By comparing with a single ground, swirling flow created by multiple ground effect spreads wider over the surface of sample. This causes temperature of the sample to increase faster. It is found from flow visualization that behaviors of swirling flow obtained by smoke incense technique and simulation have a good agreement. Furthermore, enhancement of heat transfer in the sample depended on the arrangement of electrode and ground, as well as, the position of the sample.

1. Introduction

The increasing necessities for saving energy and environmental concerns have prompted the development of more effective heat transfer equipment with enhanced heat transfer rates. The flow in channel occupies an important place among the several heating systems [1–7]. One way to achieve considerable improvement in thermal efficiency is to extend heat transfer area and increase the flow velocity [8–10]. The convective heat transfer enhancement technique utilizing electrostatic force generated from the polarization of dielectric fluid or Electrohydrodynamic (EHD) can be one of the most promising methods among various active techniques because of its several advantages, for examples, a quick response to the flow control, a significant increase in the convection heat transfer, simplified implementation using only a small transformer and electrodes and a small consumption of electric power.

Mechanism of Electrohydrodynamic method is explained by Fig. 1. When electrical voltage is introduced to airflow, ions from a sharp electrode move forwards to the ground electrode, i.e. Corona wind [11]. As a result, the momentum of airflow is enhanced. Meanwhile, shear flow effect which is occurred by velocity difference between charged and uncharged air, induces the uncharged air to become swirling flow. This technique deals to the interdisciplinary field with subjects concerning the interactions between electric, flow, and temperature fields. In order to improve convective heat transfer, some researchers studied seriously in Electrohydrodynamic process [12–16]. Kasayapanand [12] studied heat transfer enhancement using Electrohydrodynamic technique for channel installing multi-electrode bank arrangements. The results showed that the electrode bank arrangement which obtained the best heat transfer performance was expressed incorporating with the optimum electrode distance ratio (transverse and longitude pitches). Moreover, the heat transfer enhancement was also depended on the number of electrodes per length and the channel dimensions. Huang and Lai [15] investigated the water evaporation enhanced by Corona wind. The Corona wind was generated by a wire electrode charged at a high dc voltage. The numerical results showed that water evaporation was able to be greatly enhanced by Corona wind. However, a cross-flow with a high velocity may diminish the effect of Corona wind. When the results were compared to experiments, the agreement was found to be reasonable, which indicated that the model had correctly represented the physical system. The discrepancy between numerical and experimental results was attributed to the variation of ambient conditions and the uncertainty in the electric properties of the media used in the numerical simulations. Chaktranond and

* Corresponding author. Tel.: +66 2 564 3001x3144.
E-mail address: cchainar@engr.tu.ac.th (C. Chaktranond).

0017-9310/$ - see front matter © 2013 Published by Elsevier Ltd.
http://dx.doi.org/10.1016/j.ijheatmasstransfer.2013.04.010

Nomenclature

b	ion mobility (m^2/Vs)
C_p	specific heat capacity (J/K)
D	electric flux density (C/m^2)
E	electric field (V/m)
EHD	electrohydrodynamic
f_E	electric force (C/m^2 s)
H	height of channel (m)
h	distance between electrode and ground in the vertical direction (cm)
J	current density (A/m^2)
k	thermal conductivity (W/m K)
L	length of channel (m)
l	distance between electrode and ground in the horizontal direction (cm)
n	outward normal from medium and coordinate in x and y axis
P	pressure (N/m^2)
q	space charge density (C/m^3)
S	sample
T	uniform temperature (K)
T_α	ambient temperature (K)
t	time (hr)
u	airflow velocity (m/s)
V	electrical voltage (V)
x, y	axis

Greek letters

ε	dielectric permittivity (F/m)
η	kinematics viscosity (m^2/s)
μ	viscosity (kg/m s)
ρ	density (kg/m^3)
ϕ	porosity (–)
κ	permeability (m^2)

Subscripts

d	lower interface
eff	effective value
i	inlet
l	liquid phase
s	sample
s	solid phase
u	upper interface
0	atmospheric, initial and wire

Superscript

T	transpose of matrix

Rattanadecho [16] experimentally investigated the influences of electrical voltage on the heat and mass transfer in porous packed bed subjected to Electrohydrodynamic drying. The four wire electrodes and a wire ground were installed in the normal flow direction and cross flow direction, respectively. Electrical voltage was applied in the range of 0–15 kV. Average velocity and temperature of hot-airflow were controlled at 0.33 m/s and 60 °C, respectively. The results showed that the heat and mass transfer rates in the packed bed were increased. The convective heat transfer coefficient and drying rate were considerably enhanced with the strength of electric fields influencing Corona wind.

In order to consider flow phenomena or flow characteristic, measurements were performed to visualize the flow pattern. For the past decade, incense smoke techniques for investigating flow visualization of the EHD have been applied, in order to analyze the modifications of flow when it perturbed with an EHD effect. It is studied by some researchers, but very short time exposure pictures of Corona wind were captured. Recently, our research group has tried to numerically investigate Corona wind subjected to EHD effect, such as Saneewong Na Ayuttaya et al. [17] carried out on the numerical simulation for the effect of ground arrangements on swirling flow in a rectangular duct subjected to Electrohydrodynamic. The result shows that, airflow of plate ground was widely swirled and extended more than with wire ground but wire ground can strongly induced the swirling flow to the local place. In case of wire ground, the strength of local fields seemed to be very interesting in the way that the technique might be used in some applications that required the local strength of Corona wind and velocity field, etc. Saneewong Na Ayuttaya et al. [18] numerically explored the influences of electrode arrangements and the number of electrodes on the fluid flow under electric field. When the distance between electrode and ground in the vertical direction $(h) \neq 0$ cm, swirling flow is occurred and its direction depended on location of h. The distance between electrode and ground in the horizontal direction (l) becomed closer, size of swirling becomes smaller but vorticity is stronger. This is because of higher and denser electric field intensity. With increasing the number of electrodes, electric field increased. This causes swirling to be larger and more violent.

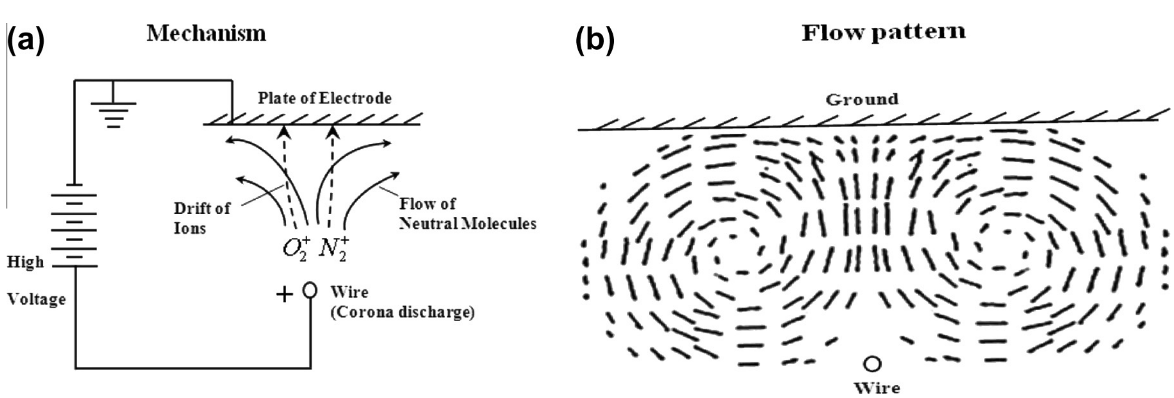

Fig. 1. Mechanism of Corona wind: (a) Mechanism of high electrical voltage (b) Corona wind pattern [11].

By comparing flow visualization, simulation results had good agreement with experiments.

Due to the complicated interactions among the electric, flow, and temperature fields on swirling flow, previous studies on Electrohydrodynamic enhanced heat transfer enhancement technique is mostly conducted by experiments. There are few numerical studies to investigate on the effect of electrically-driven swirling flow on heat transfer enhancement. Therefore, in order to provide information on the interactions of the electric, flow, and temperature fields adequately, it is essential to simulate all of these fields systematically. Based on the literature reviews [19,20], the heat transfer between a body and fluid flow, it is a conjugate problem. But there are few studies on Electrohydrodynamic technique with conjugate approach. In this study, a two-dimensional model is used to simulate the swirling flow occurred by electric force and heat transfer in specified domain. Electrical voltage and electrode arrangement, which influence swirling flow are varied. Furthermore, single and multiple grounds are investigated. In addition, the present simulation results are compared with the experimental results in order to indicate that the simulation has correctly presented. Finally, enhancement of heat transfer is explored by investigating the temperature of a saturated porous material placed under the channel.

2. Computational domains

The computational domains are shown in Fig. 2 and compose of main three parts: the first and second parts are fluid flow and heat transfer domains, dimensions of channel are 2.0 m long × 0.15 m high. The third part is electric field domain. In order to calculate electric field penetrating through on channel flow the dimensions of the electric field domain are 2.0 m long and 0.8 m high. A position of single ground is shown in Fig. 2. When focus to the plane of electrode number (n) and single ground, $n = 1$, 3 and 5 are arranged in Fig. 3(a)–(c), respectively. In addition, Fig. 4(a)–(c) is arranged in $n = 1$, 3 and 5, respectively when focus to the plane of electrode number (n) and multiple grounds. In this simulation, electrode and ground wires are assumed to be a circle with a diameter of 0.5 mm. Space charge densities (q_0) at the tip of electrode is considered from Griffiths [21], of which most of the corona current is collected at the wires. Position of single ground is always fixed at $x = 0$ m and $y = 0$ m while distance between electrode and ground are varied in the horizontal (l) and vertical (h) directions. In order to study effect of Corona wind on the enhancement of heat transfer, a saturated porous sample (S) of 15 cm × 5 cm is attached under the bottom wall surface.

2.1. Analysis of electric field in a channel flow

Mathematical model is developed to predict the electric field. To simplify the problem, the dielectric property is constant and the effect of magnetic field is negligible.

Electric field distribution is computed from Maxwell's equations listed as below:

$$\nabla \cdot \varepsilon \vec{E} = q, \tag{1}$$

$$\vec{E} = -\nabla V, \tag{2}$$

$$\nabla \cdot J + \partial q / \partial t = 0, \tag{3}$$

$$J = qb\vec{E} + q\vec{u}, \tag{4}$$

where $\vec{E}$ is electric field intensity, q is the space charge density in the fluid, ε is dielectric permittivity, V is electrical voltage, J is current density, b is ion mobility, t is time and $\vec{u}$ is airflow velocity. The governing equation for computing the electric force per unit volume (f_E) performing on fluid flow can be expressed as Landau and Lifshitz [22]

$$\vec{f}_E = q\vec{E} - \frac{1}{2}\vec{E}^2 \nabla\varepsilon + \frac{1}{2}\nabla\left[\vec{E}^2\left[\frac{\partial\varepsilon}{\partial\rho}\right]_T \rho\right], \tag{5}$$

where ρ is density of fluid. Simply described, three terms on the right-hand side of Eq. (5) represent the electrophoretic, dielectrophoretic and electrostrictive forces, respectively. The electrophoretic force or Coulomb force results from the net uncharged within the fluid or ions injected from the electrodes. The interactions within the individual phases are typically associated with this component. The dielectrophoretic force is a consequence of inhomogeneity or spatial change in the permittivity of the dielectric fluid due to non-uniform electric field, temperature gradients and phase differences. Lastly, the electrostrictive force is caused by non-homogeneous electric field strength and the variation in dielectric constant with temperature and density. In addition, the model assumes that dielectric properties are constant and homogeneity. Furthermore, magnetic field effect is neglected. Therefore, the second and third terms on the right- hand side of Eq. (5) are negligible. Consequently, Eq. (5) reduces to

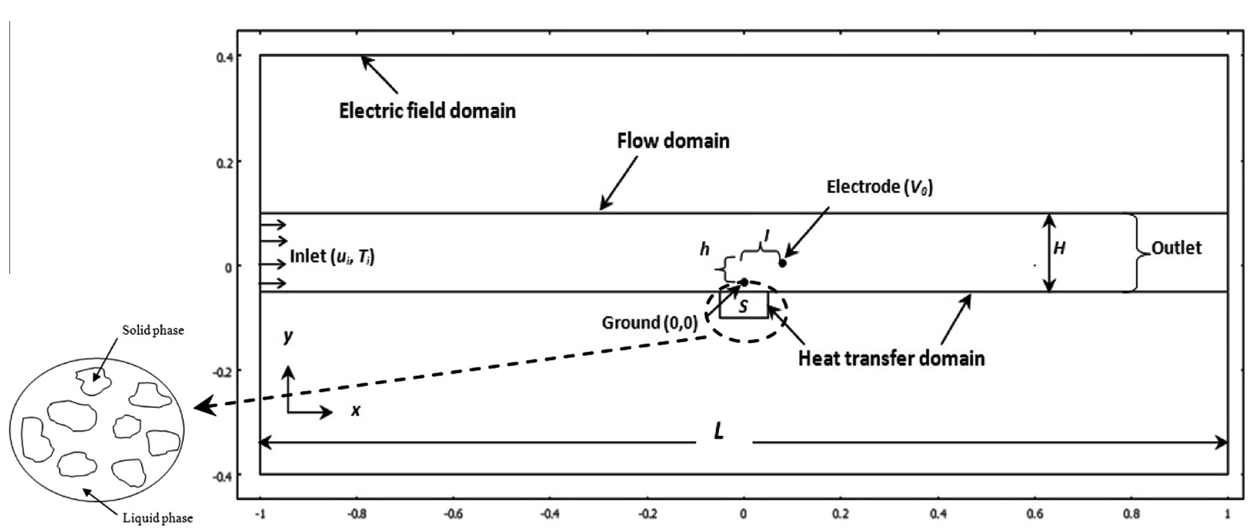

Fig. 2. Computational domain of single ground arrangement.

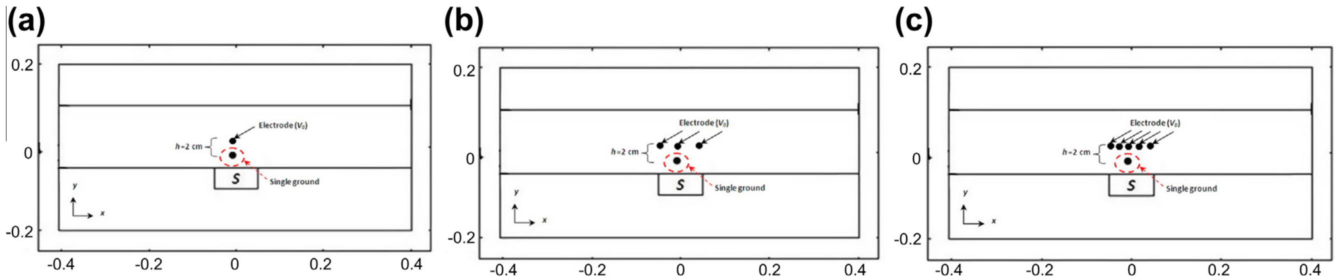

Fig. 3. Computational domains of single ground arrangement when (a) $n = 1$ (b) $n = 3$ and (c) $n = 5$.

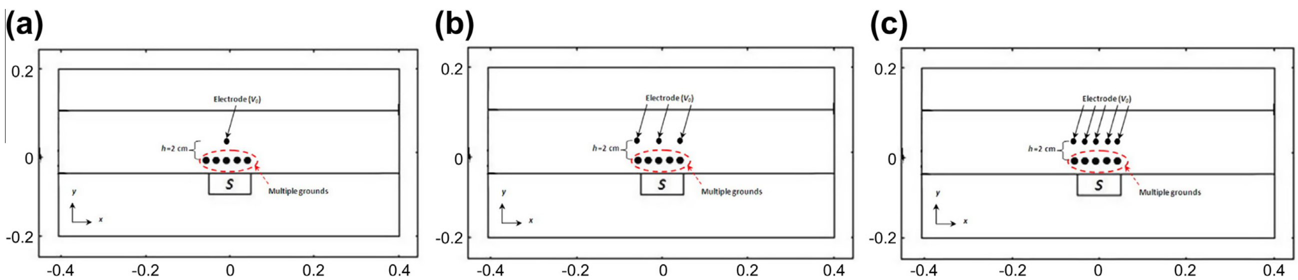

Fig. 4. Computational domains of multiple grounds arrangement when (a) $n = 1$ (b) $n = 3$ and (c) $n = 5$.

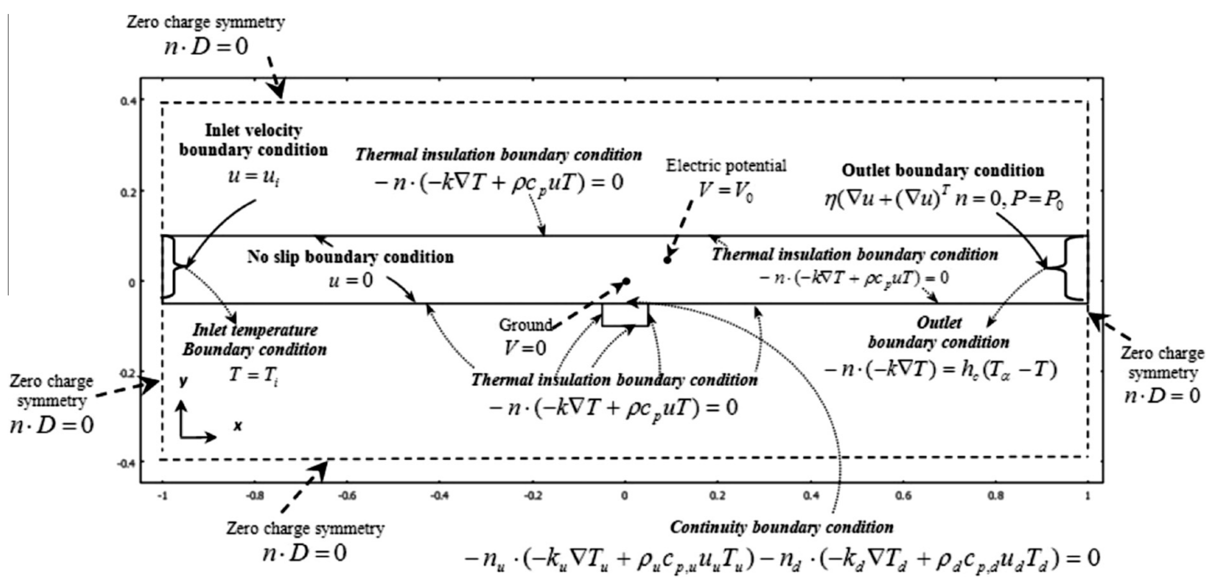

Fig. 5. Boundary conditions used in analysis.

$$\vec{f}_E = q\vec{E}, \tag{6}$$

Electric field distribution is emitted from electrode wire and induces to the ground. Therefore, normal font for the boundary conditions for solving electric field, as shown in Fig. 5, it is described as follows:

The outer sides of the boundary condition are considered as zero charge symmetry,

$$n \cdot D = 0, \tag{7}$$

where n is the outward normal from medium and D is electric flux density. Electrode and ground are considered as electrical voltage and ground boundary condition, respectively

$$V = V_0 \quad \text{at electrode position} \tag{8}$$

$$V = 0, \quad \text{at ground position} \tag{9}$$

where subscript zero means at electrode wire.

2.2. Analysis of flow field in a channel flow

In order to simplify the problem, the air is a single phase, the fluid physical properties are assumed to be constant and flow is incompressible. The boundary condition is solved the swirling flow, as shown in Fig. 5. The continuity and Navier–Stokes equations which coupled with Coulomb force equation are expressed as:

$$\nabla \cdot \vec{u} = 0, \tag{10}$$

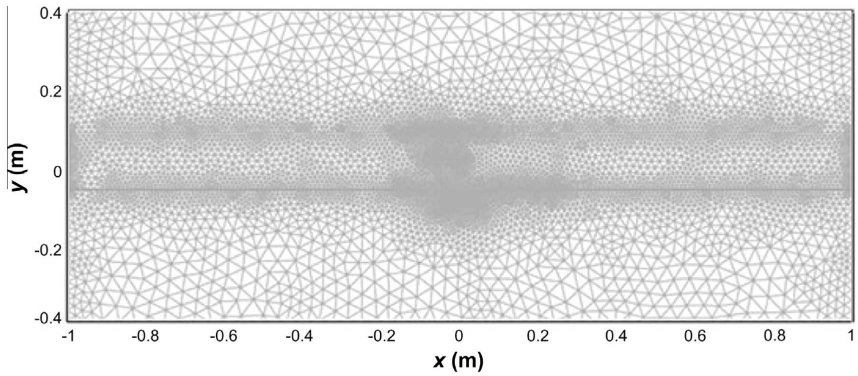

Fig. 6. Two-dimensional finite element meshes of flow, temperature and electric field domains.

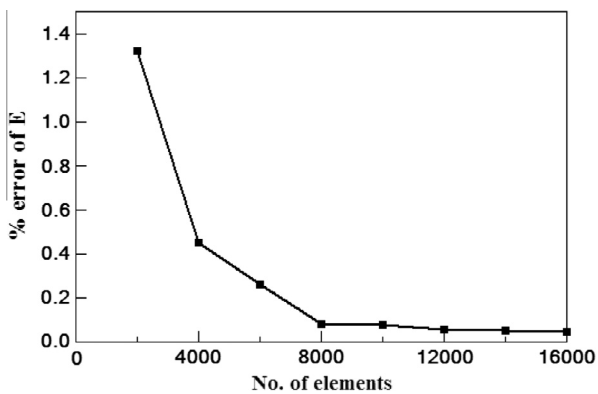

Fig. 7. Grid validation.

Table 1
Flow properties.

Modeling parameter	Value
Ion mobility, b	$1.80 \times 10^{-4}\,\mathrm{m^2/Vs}$
Initial temperature, $T(t_0)$	60 °C
Inlet velocity, u_i	0.35 m/s
Dielectric permittivity, ε	$8.85 \times 10^{-12}\,\mathrm{F/m}$
Kinematics viscosity, η	$1.76 \times 10^{-5}\,\mathrm{m^2/s}$
Density, ρ	$1.060\,\mathrm{kg/m^3}$

Table 2
Saturated porous medium properties [24].

Modeling parameter	Value
Porosity of solid, ϕ	0.385
Permeability of solid, κ_s	$8.41 \times 10^{-12}\,\mathrm{m^2}$
Density of solid, ρ_s	$2500\,\mathrm{kg/m^3}$
Specific heat of solid,C_{ps}	0.80 kJ/(kg K)
Density of liquid, ρ_l	$1000\,\mathrm{kg/m^3}$
Specific heat of liquid, C_{pa}	4.186 kJ/(kg K)
Initial temperature of sample, $T_s(t_0)$	25 °C
Water saturation	1

$$\rho\left[\frac{\partial \vec{u}}{\partial t}+(\vec{u}\cdot\nabla)\vec{u}\right]=-\nabla\vec{P}+\mu\nabla^2\vec{u}+\vec{f}_E, \tag{11}$$

where P is pressure, and μ is viscosity of air. As shown in Eq. (12), the inlet velocity boundary condition is defined as

$$\vec{u}=\vec{u}_i, \tag{12}$$

The uniform inlet velocity (u_i) of air is fixed at 0.35 m/s. The pressure of outlet boundary condition is considered with no viscous stress. This boundary condition specifies vanishing viscous stress along with a Dirichlet condition on the pressure:

$$\eta(\nabla\vec{u}+(\nabla\vec{u})^T\cdot n=0 \text{ and } \vec{P}=\vec{P}_0, \tag{13}$$

where η is dynamic viscosity, P_0 is atmospheric pressure and T is transpose of matrix. The upper and lower of channel flow are considered as no slip boundary condition, this is the standard and default boundary condition for a stationary solid wall. The condition prescribes

$$\vec{u}=0 \tag{14}$$

2.3. Analysis of heat transfer in a channel flow

Apart from the effect of swirling flow, heat transfer in a channel and a sample are analyzed. The validity of the following statements is also considered:

(1) The effect of buoyancy is negligible.
(2) The thermal property of the fluid is considered to be constant.
(3) No emission or absorption of radiant energy is occured.
(4) The saturated porous medium is considered to be isotropic and homogeneous.
(5) Saturation of porous medium is fixed at 1.

The boundary conditions used for the heat transfer, there are shown in Fig. 5.

Temperature distribution is calculated by energy equation,

$$\rho C_p\left[\frac{\partial T}{\partial t}+\vec{u}\,\nabla T\right]=k(\nabla^2 T) \tag{15}$$

where C_p is the specific heat capacity and k is thermal conductivity. To solve the temperature distribution, the inlet and outlet boundary conditions are shown in Eqs. (16) and (17), respectively which defined as

$$T=T_i, \tag{16}$$

and

$$-n\cdot(-k\nabla T)=h_c(T_\alpha-T), \tag{17}$$

where h_c is convective heat transfer coefficient ∇T is temperature gradient. The uniform initial temperature ($T(t_0)$) of hot-airflow is

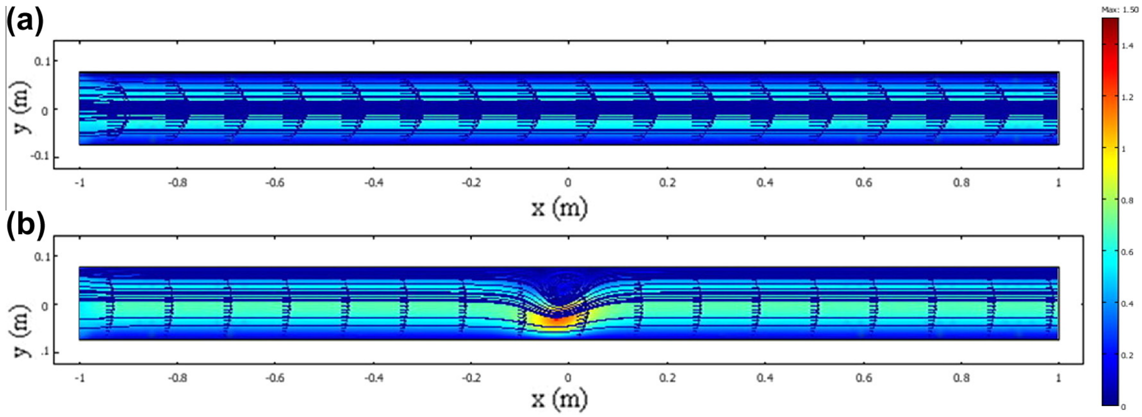

Fig. 8. Present simulated results of swirling flow along x–y plane (h = 1 cm, l = −2 cm and u_i = 0.35 m/s): (a) without electric field (b) V_0 = 15 kV.

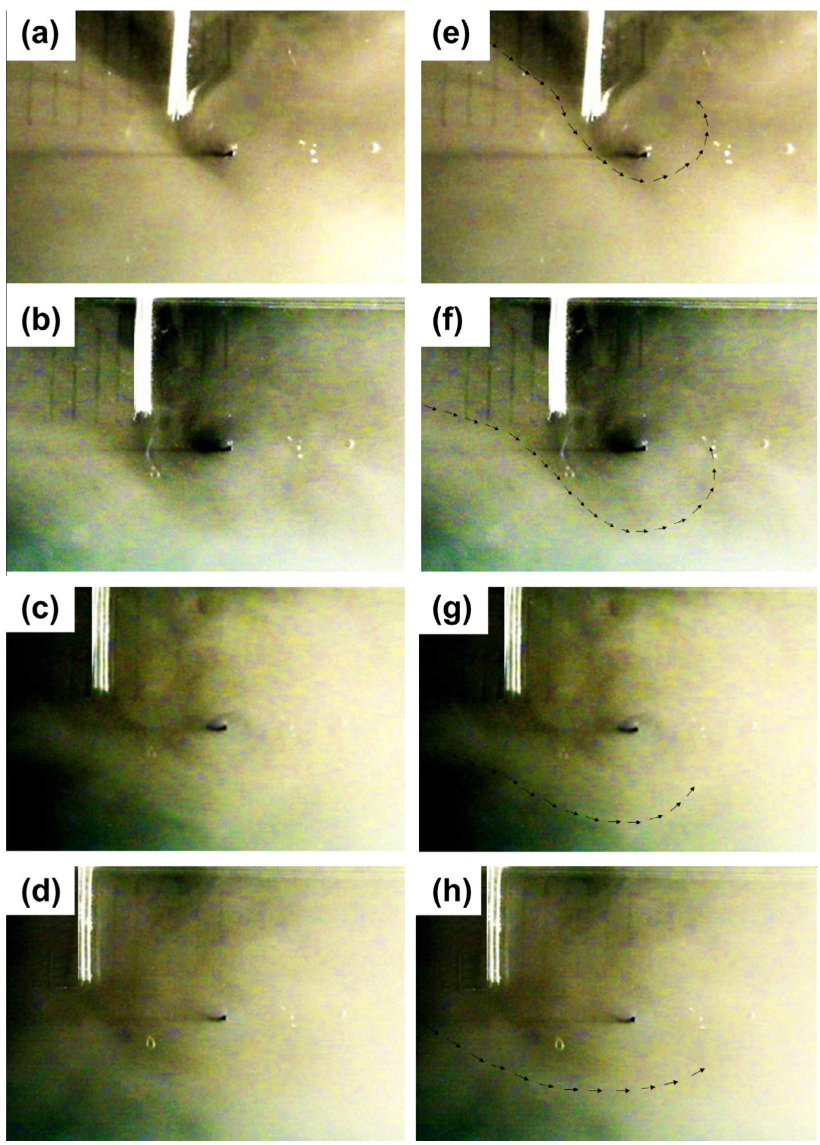

Fig. 9. Experimental result of swirling flow in various l when V_0 = 15 kV, $\vec{u}_i$ = 0.35 m/s and h = 2 cm: (a)–(d) incense smoke technique motion when l = −2, −4, −6 and −8 cm, respectively and (e)–(h) incense smoke technique motion with vector sketch when l = −2, −4, −6 and −8 cm, respectively.

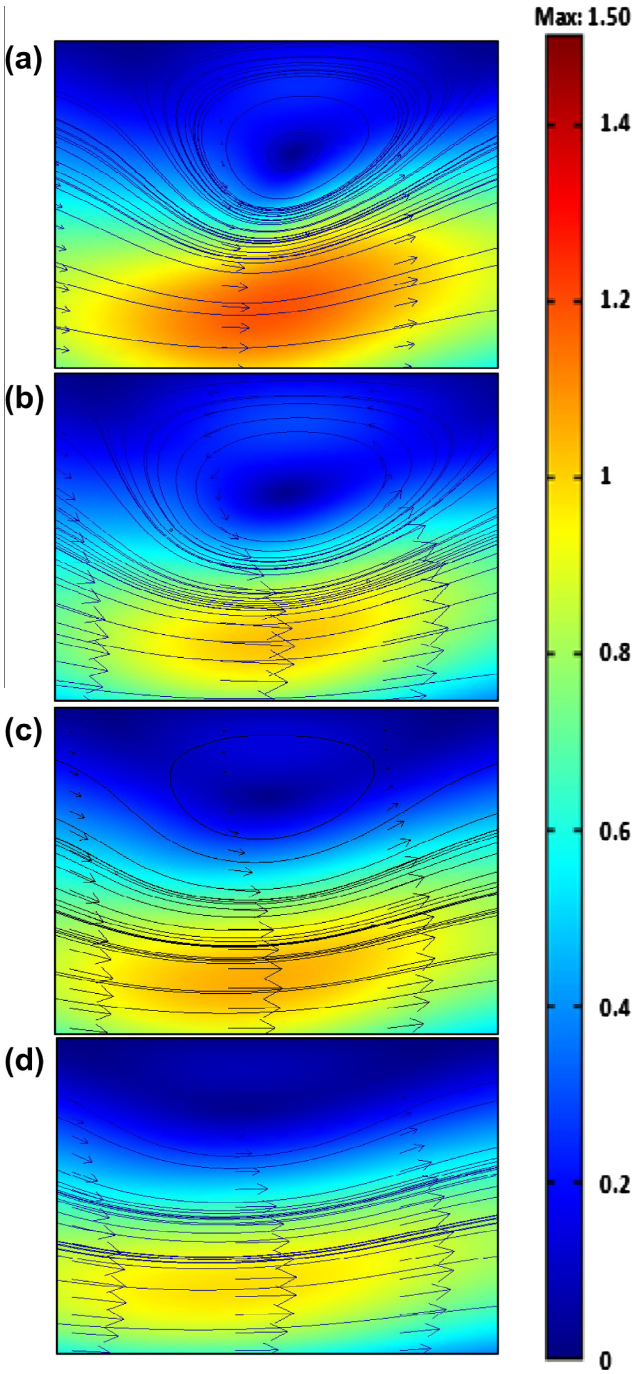

Fig. 10. Present simulation result of swirling flow in various l when V_0 = 15 kV, E_i = 0.35 m/s and h = 2 cm: (a)–(d) swirling flow when l = −2, −4, −6 and −8 cm, respectively.

60 °C. The upper and lower walls of channel are insulated. The condition prescribes:

$$-n \cdot (-k\nabla T + \rho c_p \vec{u} \nabla T) = 0, \tag{18}$$

2.4. Analysis of flow field and heat transfer in a sample

The governing equations describing the flow field and the heat transfer within the sample are calculated from Eq. (19):

$$\frac{1}{\phi}\frac{\partial \vec{u}}{\partial t} + \frac{1}{\phi^2}(\vec{u} \cdot \nabla)\vec{u} = -\frac{1}{\rho_l}\nabla P + \frac{\mu}{\rho\phi}\nabla^2 \vec{u} - \frac{\mu \vec{u}}{\rho\kappa} \tag{19}$$

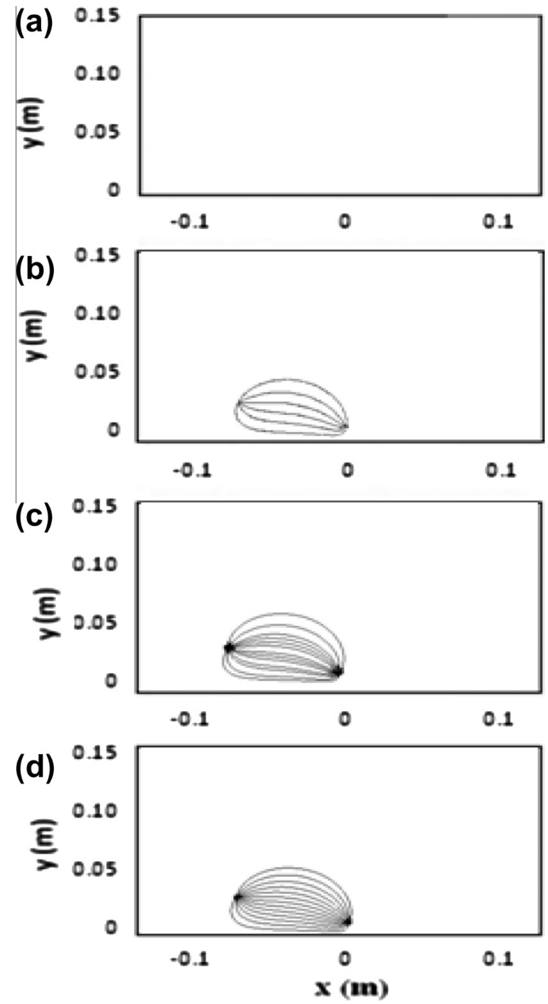

Fig. 11. Electric field in various V_0 when l = −7.5 cm and h = 2 cm: (a) V_0 = 0 kV (b) V_0 = 10 kV (c) V_0 = 20 kV and (d) V_0 = 30 kV.

and

$$(\rho C_p)_{eff}\frac{\partial T}{\partial t} + (\rho C_p)_l \vec{u} \nabla T = k_{eff}\nabla^2 T \tag{20}$$

and effective thermal conductivity (k_{eff}) in a porous medium is computed by [23]

$$k_{eff} = (1-\phi)k_s + \phi k_l, \tag{21}$$

where ϕ is porosity, κ is permeability. Subscript s and l are solid and liquid phase. The uniform initial temperature of sample ($T_s(t_0)$) is 25 °C. The only surface of the sample is exposed to hot-airflow. The other surface is considered as insulated boundary condition

$$-n \cdot (-k\nabla T) = 0, \tag{22}$$

where n is normal unit vector. It is evident that a generalized conjugate approach to the combined heat and fluid flow process, the interface of air and sample are solved by Eq. (23). It is defined as

$$-n_u \cdot (-k_u \nabla T_u + \rho_u c_{p,u} \vec{u}_u T_u) - n_d \cdot (-k_d \nabla T_d + \rho_d c_{p,d} \vec{u}_d T_d) = 0 \tag{23}$$

The upper and the lower interfaces are designated by subscript u and d, respectively.

3. Calculation procedure

In simulations, the sample is placed under the bottom wall of channel and only the upper surface of sample is exposed to hot- air-

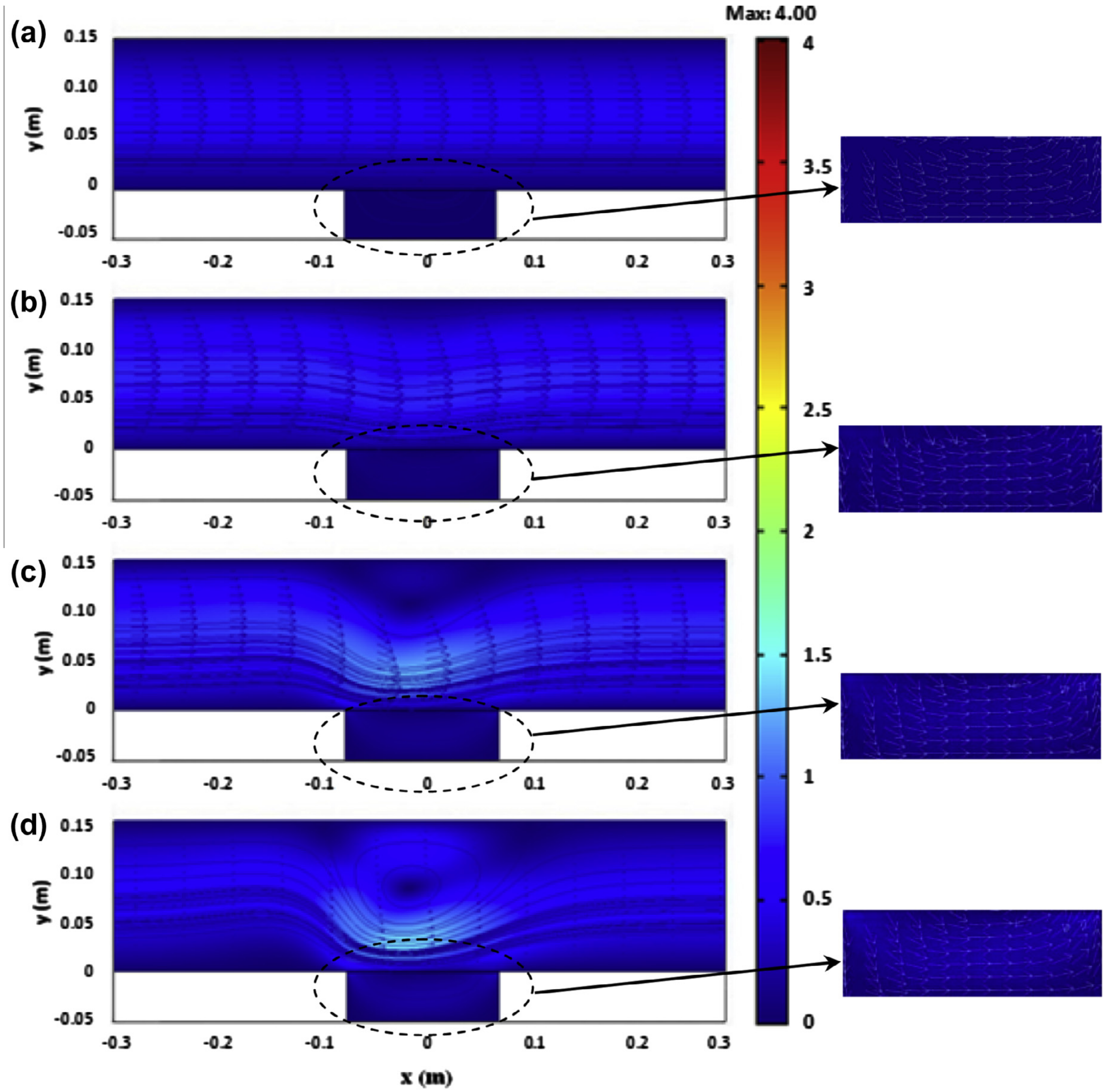

Fig. 12. Swirling flow in various V_0 when $l = -7.5$ cm and $h = 2$ cm: (a) $V_0 = 0$ kV (b) $V_0 = 10$ kV (c) $V_0 = 20$ kV and (d) $V_0 = 30$ kV.

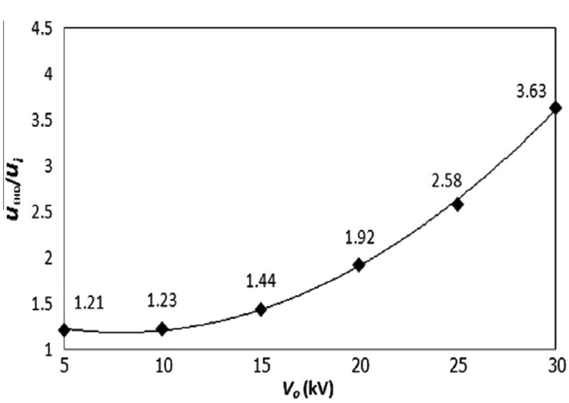

Fig. 13. Velocity ratios when various V_0 ($l = -7.5$ cm and $h = 2$ cm).

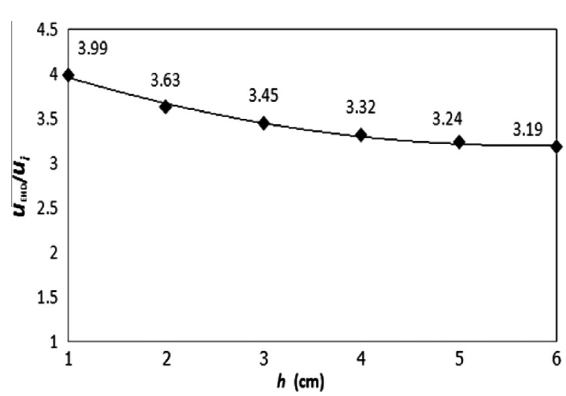

Fig. 14. Velocity ratios when various h ($l = -7.5$ cm and $V_0 = 30$ kV).

flow. In this study, the computational scheme is assembled in finite element model using a collocation method. The idea is to choose a finite-dimensional space of candidate solutions and a number of points in the domain and to select that solution which satisfies the given equation at the collocation points. In order to obtain a good approximation, a fine mesh is specified in the sensitive areas.

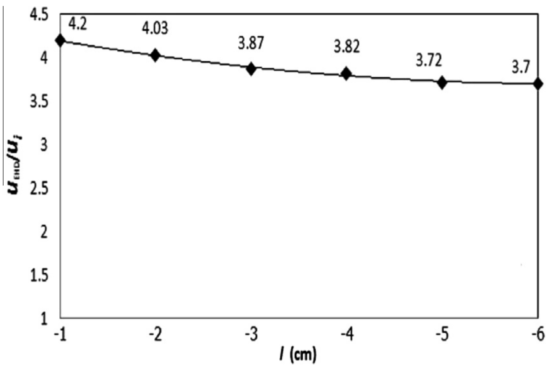

Fig. 15. Velocity ratios when various l (h = 2 cm and V_0 = 30 kV).

This study provides a variable mesh method for solving the flow, temperature and electric field problem as shown in Fig. 6. The equations are solved by using COMSOL. Lagrange quadratic element is chosen as the basic functions with triangular shapes. The system of governing equations is solved with the unsymmetrical multi-frontal method. The convergence curve resulting from the convergence test is shown in Fig. 7. This convergence test leads to the mesh with approximately 8000 elements. It is reasonable to assume that, with this element number, the accuracy of the simulation results is independent on the number of elements and therefore save computation memory and time. Higher numbers of elements are not tested due to lack of computational memory and performance.

4. Results and discussion

In the simulation, effect of electrical voltage and effect of electrode and ground arrangements are systematically investigated. A subdomain is used for the entire simulation space which made up the inside channel, where the electrical, charge transport, temperature and fluid domain equations are solved the subdomain modeling parameter values shown in Table 1. Properties of sample (saturated porous medium) are shown in Table 2 [24].

4.1. Verification of the model

In order to verify the accuracy of the present numerical model, the modified case of the simulated results is validated against the experimental data. The experimental flow visualization is based on the incense smoke technique, in order to observe the motion of airflow subjected to the electric field. A spotlight of 500 Watt is placed at the outlet of channel and the light direction is opposite to the flow direction. In addition, the motion of airflow is continuously captured by a digital video camera recorder (SONY DCR-PC108/PC109E). Fig. 8 shows present simulated results of airflow along x–y plane when h = 1 cm, l = −2 cm and the uniform inlet velocity (u_i) is controlled at 0.35 m/s. As shown in Fig. 8(a), when electric field is not included (No EHD), swirling flow cannot be observed. When electric field is considered (V_0 = 15 kV), swirling flow is clearly displayed at the location closed to the electrode and ground, as shown in Fig. 8(b).

Comparison between experiment and simulation are shown in Fig. 9 and Fig. 10. The distance between electrode and ground in

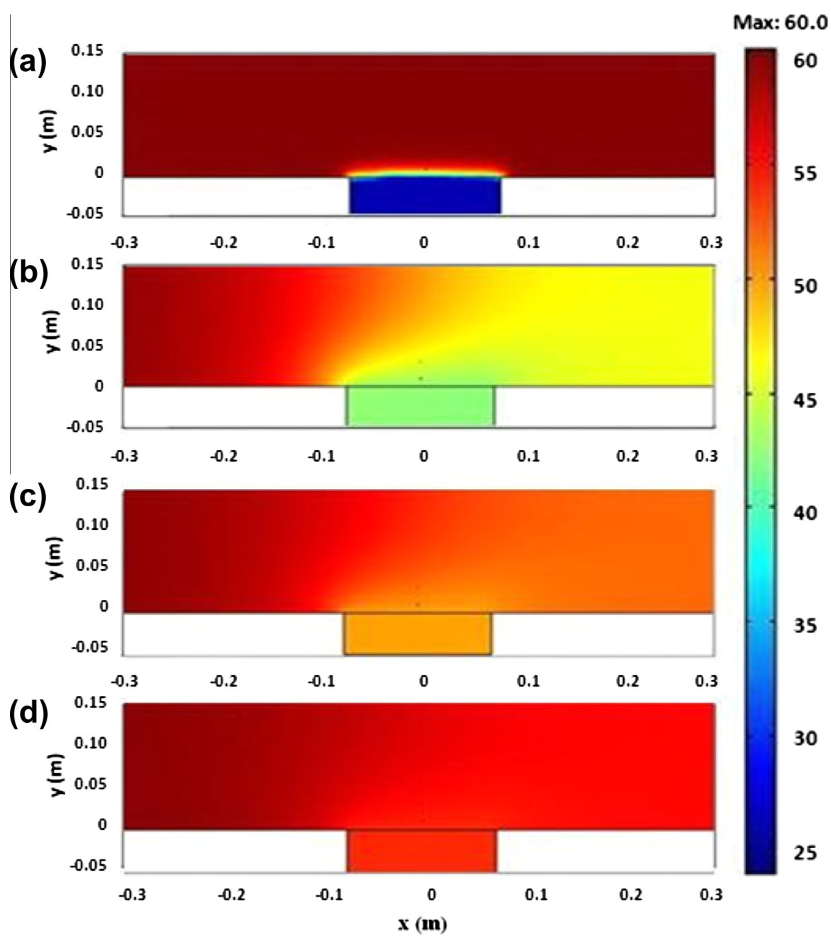

Fig. 16. Temperature distribution within sample in various time when h = 2 cm, l = 0 cm and V_0 = 30 kV: (a) t = 0 s, (b) t = 300 s, (c) t = 600 s and (d) t = 900 s.

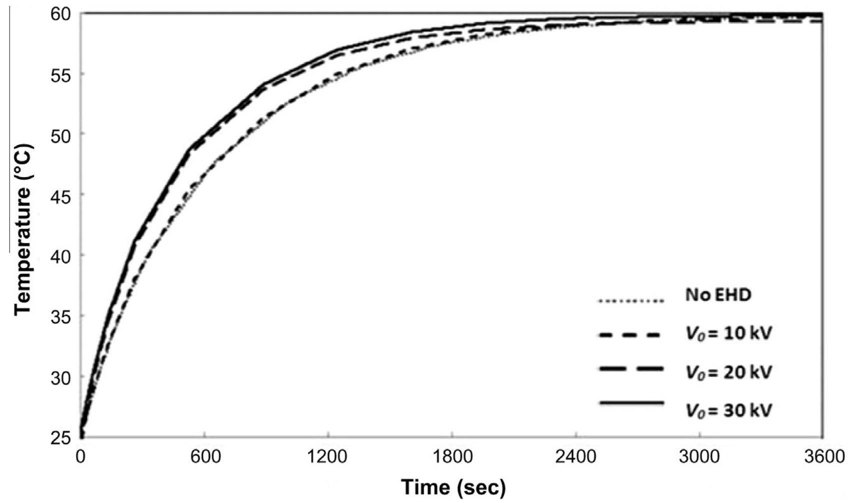

Fig. 17. Development of surface temperature in various V_0.

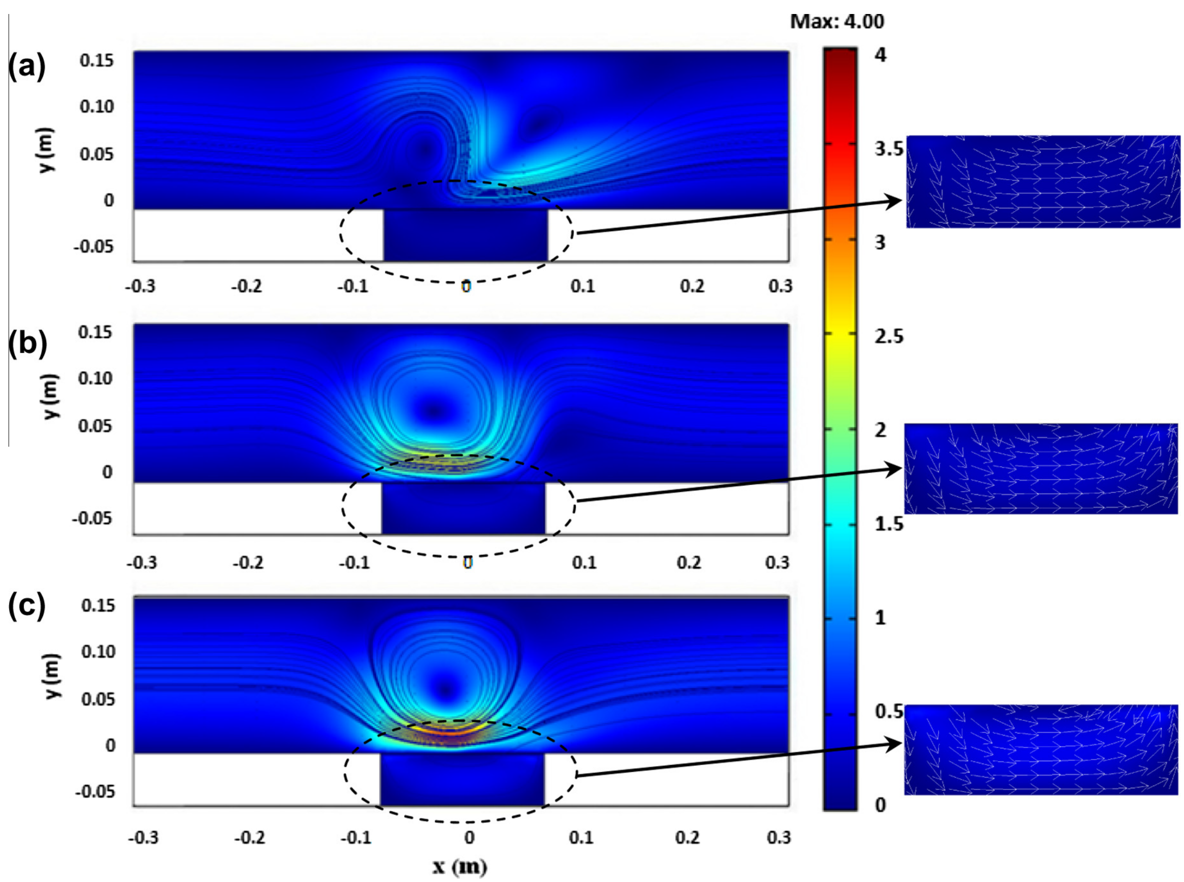

Fig. 18. Swirling flow in various n when h = 2 cm and V_0 = 30 kV: (a) n = 1 (b) n = 3 and (c) n = 5 from single ground.

the vertical direction (h) is fixed at 1 cm but the distance between electrode and ground in the horizontal direction (l) are varied from 2–8 cm. Fig. 9(e)–(h) shows swirling flow with vector form in order to clearly observe the motion from the incense smoke technique. As shown in Fig. 9(e) and Fig. 10(a), when the gap (l) becomes closer, size of swirling flow is smaller and the swirling flow is appeared above the electrode and ground. But when the gap (l) becomes larger it can be seen that the bigger swirling flow presents so the more convective surface area is obtained, as shown in Fig. 9(f) and (g) and Fig. 10(b) and (c). The density of streamline decreases because space charge is not concentrated when the gap become larger so the maximum velocity field (u_{max}) is decreased. Swirling flow in case of Fig. 9(h) and Fig. 10(d) can not been presented due to shear flow effect cannot induce the secondary flow. Furthermore, from the present simulation result, the maximum velocity field for l = −2, −4, −6 and −8 cm are 1.194, 1.117, 1.060 and 0.985 m/s, respectively. When the gap (l) becomes closer, the size of swirling flow becomes smaller.

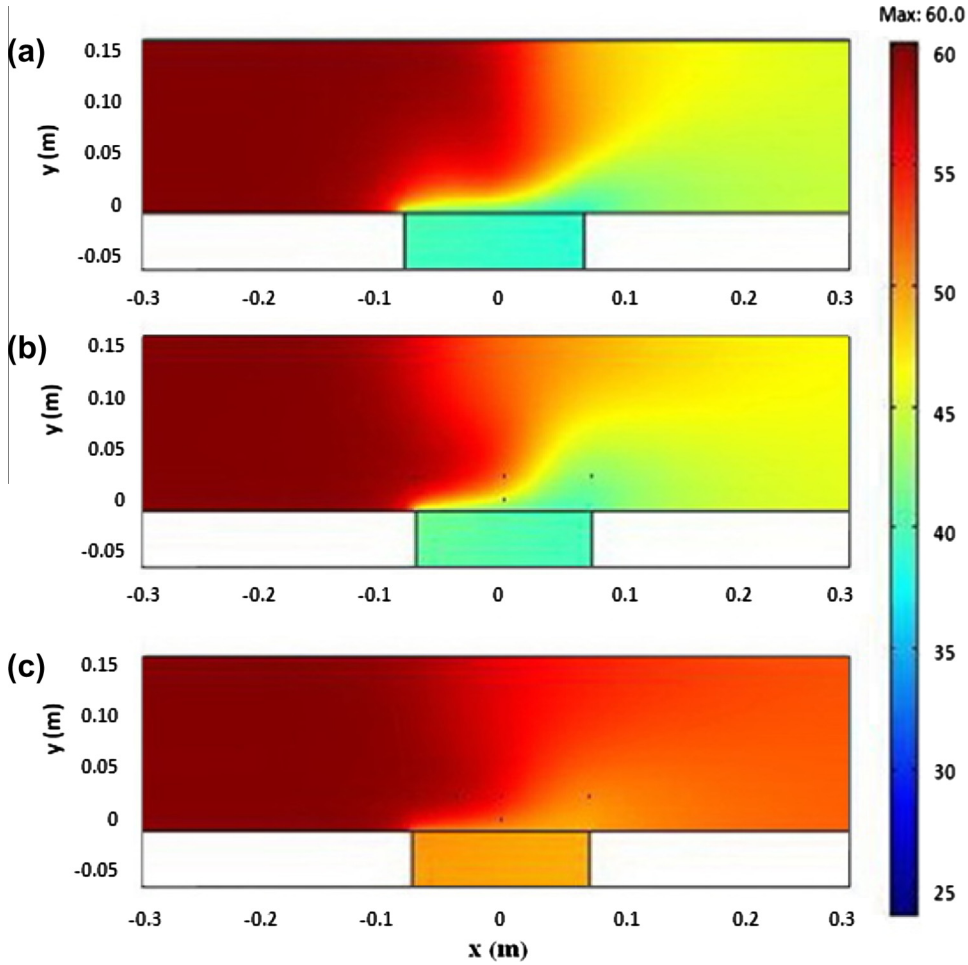

Fig. 19. Temperature distribution within saturated porous medium with various n and single ground when t = 200 s, h = 2 cm and V_0 = 30 kV (a) n = 1 (b) n = 3 (c) n = 5.

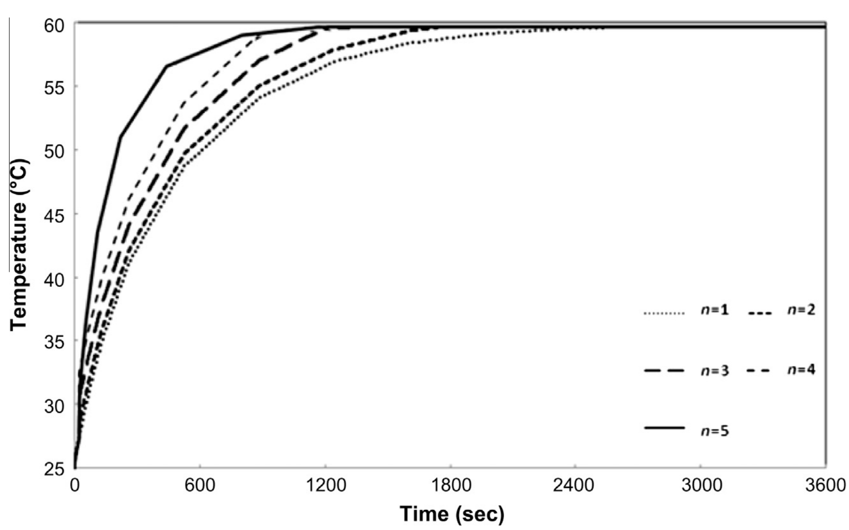

Fig. 20. Relationship between surface temperature of sample and time when single ground in various n.

4.2. Effect of single electrode on fluid flow and heat transfer in a sample

To investigate the effect of a single ground, the ground arrangement is done by following the Fig. 2. In all cases, the inlet velocity (u_i) is fixed at 0.35 m/s and the distance between electrode and ground in the vertical direction or gap (h) and the horizontal direction or gap (l) are fixed at 2 cm and −7.5 cm, respectively. Fig. 11 show electric field from single electrode. When electrical voltage are applied (Fig. 11(b)–(d)), it can be seen that the electric field moves outwardly from electrode to ground and it is concentrated at both electrode and ground. Furthermore, electric field is more

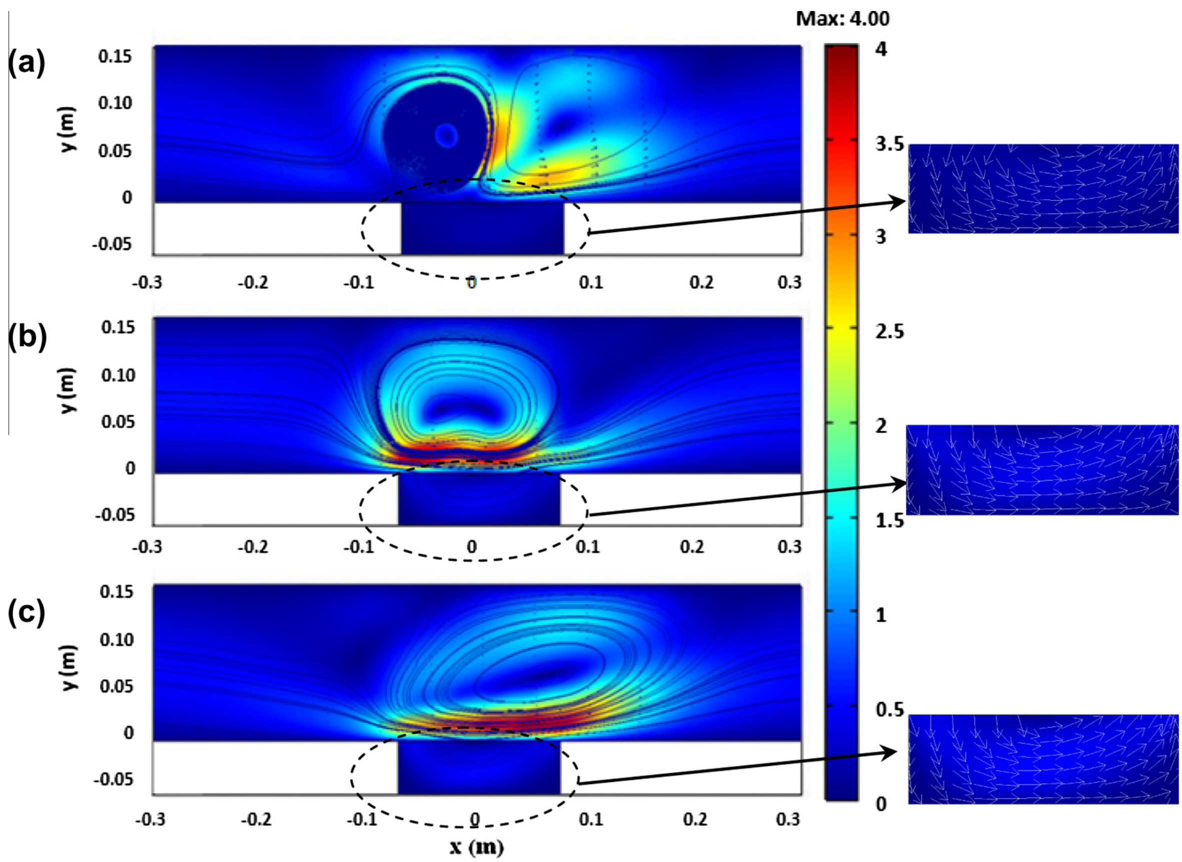

Fig. 21. Swirling flow in various n when h = 2 cm and V_0 = 30 kV: (a) n = 1 (b) n = 3 and (c) n = 5 from multiple grounds.

concentrated when higher electrical voltage is applied and the characteristic of electric field is the same pattern in each case. These field lines can be used as representative of fluid motion driven by Coulomb force. So Coulomb force changes the flow pattern. In addition, the effects of shear flow to become the swirling flow. Fig. 12 illustrates the swirling flow patterns in various electrical voltages from 0 to 30 kV. As shown in Fig. 12(a), when No EHD (V_0 = 0 kV), swirling flow is not presented. When electric field is applied, as shown in Fig. 12(b)–(d), the shear flow induces the neutral airflow, resulting in the occurrence of distorted and swirling flows. With increasing the electrical voltage, fluid velocity near sample surface is more increased.

Normally, heat transfer can be enhanced by increasing the velocity of hot-airflow. The velocity ratio is defined as maximum velocity with EHD to maximum velocity without electric force, i.e. u_{EHD}/u_i. As shown in Fig. 13, the velocity ratio depends on electrical voltages. In other words, the velocity ratio is proportional to square of electrical voltage, i.e. $u_{EHD}/u_i \propto V_0^2$..

Fig. 14 shows the maximum velocity of air is enhanced by EHD when V_0 = 30 kV and l is fixed at −7.5 cm. It can be seen that when the gap (h) become closer, the velocity ratio increases significantly or $u_{EHD}/u_i \propto h^{-2}$. Furthermore, V_0 and h are fixed at 30 kV and 2 cm, respectively. As shown in Fig. 15, the velocity ratios increases significantly when the gap (l) become closer or $u_{EHD}/u_i \propto l^{-2}$. This is because Coulomb force is inversely proportional to square of gap. As such charged airflow decreases significantly when the gap becomes farther and the effect of shear flow is decreased.

Fig. 16 shows variation of temperature when initial temperature of air and sample are 60 °C and 25 °C, respectively. For interface zone, the variation of temperatures is treated with parabolic function. When time progresses, heat from airflow transfers within sample so the temperature of airflow is decreased. Heat transfer rate becomes lower, this causes temperature at the sample surface gradually increases when temperature of sample closes to temperature of airflow. Fig. 17 shows development of surface temperature of sample in various electrical voltages. Increasing electrical voltages much more speed up the surface temperature of sample to close to airflow temperature.

4.3. Effect of the electrode number (n) and single ground on swirling flow

Arrangement of a single ground is shown in Fig. 3. In Fig. 18, it shows behaviors of airflow in various the electrode number (n) when gap h = 2 cm and V_0 = 30 kV. When n = 1, double cells of swirling flows are appeared. The front cell is more clearly notice than the latter cell due to the front cell is supported from the inlet airflow so the latter cell is smaller than the front cell. When the electrode number increases, electric field is more concentrated at the single ground. It can be seen that one cell is combined from front and latter cells due to increasing the electrodes. Furthermore, size of swirling flow in Fig. 18(c) is bigger than Fig. 18(b), due to high electric field intensity influences shear flow resulting the enhancement of swirling flow. With increasing the electrode number, fluid velocity near single ground is more increased. The maximum velocity field of multiple electrodes is totally higher than that of single electrode. This is because the effect of multiple electrodes can strongly induce the swirling flow to the local ground.

Temperature distribution within sample in various electrode numbers (n) is considered in Fig. 19 when t = 200 s, h = 2 cm. Temperature within sample is increased by increasing electrode num-

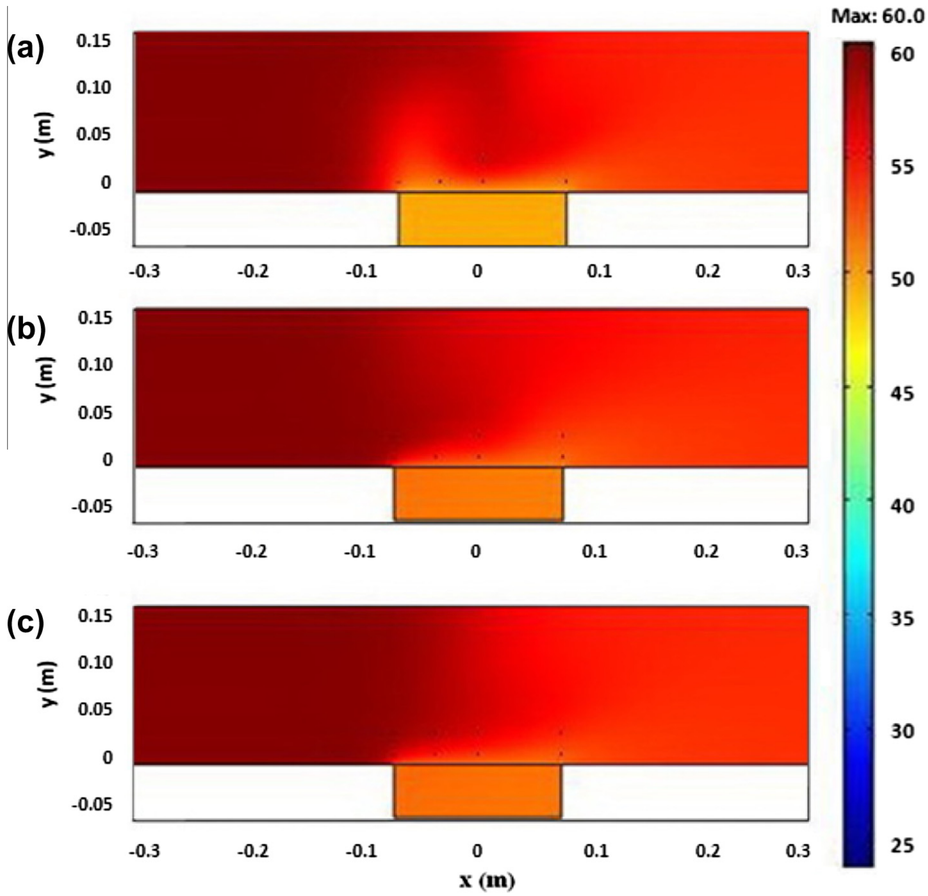

Fig. 22. Temperature distribution within saturated porous medium with various n and multiple grounds when $t = 200$ s, $h = 2$ cm and $V_0 = 30$ kV (a) $n = 1$ (b) $n = 3$ (c) $n = 5$.

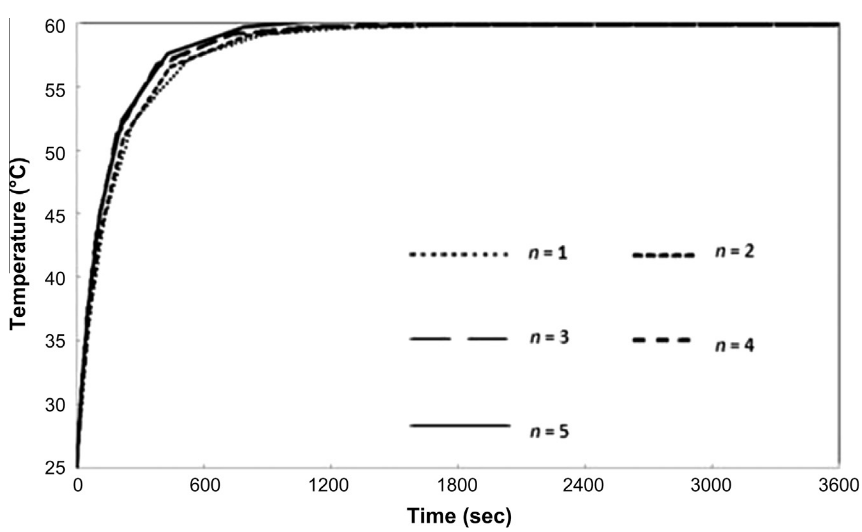

Fig. 23. Relationship between surface temperature of sample and time with various n.

ber. When increasing the electrodes, stronger swirling flow influences heat transfer within sample. Fig. 20 shows the relationship of the temperature in various electrode numbers (n) and time. As explained before, increasing electrical voltage causes strength of swirling flow to be stronger. With swirling flow effect, fluid flow above the sample surface moves faster and then leads the heat to more transfer to the sample surface. This causes the temperature of sample to rapidly increase.

4.4. Effect of the electrode number (n) and multiple grounds on swirling flow

Arrangement of the multiple grounds arrangement is shown in Fig. 4. In Fig. 21, it shows behaviors of swirling flow in various the electrode numbers (n) when $h = 2$ cm and $V_0 = 30$ kV. When $n = 1$, double cells of swirling flow are appeared. However, the latter cell is still smaller than the front cell due to behavior of swirling flow is usually circulated around the ground [16] so the front cell is induced from the multiple grounds and the swirling flow from front cell is more concentrated than the latter cell. When the electrode number increases, one cell is combined from front and latter cells. Electric field is concentrated at the multiple grounds so shear flow effect causes fluid velocity near sample surface to be increased. It can be seen that size of swirling flow in Fig. 21(c) is bigger than Fig. 21(b), because high electric field conducts high shear flow resulting the enhancement of swirling flow. Furthermore, multiple grounds can induce electric force more than single ground so the swirling flow can spread over the sample surface.

The liquid flow pattern in saturated porous sample is shown in Figs. 12, 18 and 21. In the all cases, the liquid flow patterns are similar. Liquid flow is affected by the swirling flow effect. With the effect of airflow velocity above the sample surface, the liquid is faster.

Fig. 22 shows temperature distribution within sample in various electrode numbers (n) when t = 200 s, h = 2 cm. Temperature within the sample is rapidly increased with increasing electrode number. Fig. 23 shows the relationship of the temperature in various electrode numbers. Increasing electrode number causes strength of swirling flow to be stronger. With high swirling flow, fluid flow above the sample surface moves faster and then leads the heat to more transfer to the sample surface. This causes the temperature of sample to rapidly increase. Furthermore, trend of temperature distribution in Fig. 23 is steeper than that case of temperature distribution in Figs. 17 and 20, so multiple grounds arrangement are more influenced than applied high voltage and electrode number.

5. Conclusion

1. The electrically-driven airflow velocity depends on electrical voltage (V_0) and the distance (gap) between electrode and ground (l and h). The strength of swirling flow becomes bigger when the electrical voltage increases. The electrically-driven of airflow velocity is proportional to square of electrical voltage ($u_{EHD}/u_i \propto V^2$) and airflow velocity is inversely proportional to square of gap or $u_{EHD}/u_i \propto h^{-2}$ and $u_{EHD}/u_i \propto l^{-2}$. However, the size of swirling flow becomes bigger when the gap is larger.
2. Effect of electrode and ground arrangement influences the fluid flow velocity within saturated porous medium and heat transfer more than increasing electrical voltage.
3. Effect of multiple grounds can induce electric force more than that of single ground so the swirling flow can spread over the sample surface. Furthermore, temperature within sample of multiple grounds more rapidly increases than single ground.

Acknowledgement

The authors would like to express their appreciation to the National Research University Project of Thailand Office of Higher Education Commission, National Research Council of Thailand and Thammasat University for their support of this study.

References

[1] Y. Mori, Y. Uchida, Forced convection heat transfer between horizontal flat plates, Int. J. Heat Mass Transfer 9 (1966) 803–817.
[2] F.P. Incropera, A.J. Knox, J.R. Maughan, Mixed convection flow and heat transfer in the entry region of a horizontal rectangular duct, Energy Citations Database 109 (1987) 434–439.
[3] A. Yabe, Y. Mori, K. Hijikata, Active heat transfer enhancement by utilizing electric fields, Annu. Rev. Heat Transfer 7 (1996) 193–244.
[4] T.I.J. Goodenough, P.W. Goodenough, S.M. Goodenough, The efficiency of corona wind drying and its application to the food industry, J. Food Eng. 80 (2007) 1233–1238.
[5] A.O. Ahmedou, M. Havet, Assessment of the electrohydrodynamic drying process, Food Bioprocess Technol. 2 (2009) 240–247.
[6] W. Cha-um, P. Rattanadecho, W. Pakdee, Experimental analysis of microwave heating of dielectric materials using a rectangular wave guide (MODE: TE10) (Case study: water layer and saturated porous medium, Exp. Therm. Fluid Sci. 33 (2009) 472–481.
[7] N. Makul, P. Keangin, P. Rattanadecho, Microwave-assisted heating of cementitious material: relative dielectric properties, mechanical property, and experimental and numerical heat transfer characteristics, Int. Commun. Heat Mass Transfer 37 (2010) 1096–1105.
[8] N. Kasayapanand, T. Kiatsiriroat, EHD enhanced heat transfer in wavy channel, Int. Commun. Heat Mass Transfer 32 (2005) 809–821.
[9] L.C. Wen, J.J. Yuh, 3D Numerical heat transfer and fluid flow analysis in plate-fin and tube heat exchangers with electrohydrodynamic enhancement, Heat Mass Transfer 41 (2005) 583–593.
[10] I.S. Shivakumara, M.S. Nagashree, K. Hemalatha, Electrothermoconvective instability in a heat generating dielectric fluid layer, Int. Commun. Heat Mass Transfer 34 (2010) 1041–1047.
[11] A. Yabe, Y. Mori, K. Hijikata, EHD study of the corona wind between wire and plate electrodes, AIAA J. 16 (1978) 340–345.
[12] N. Kasayapanand, Numerical study electrode bank enhanced heat transfer, Appl. Therm. Eng. 26 (2006) 1471–1480.
[13] D.B. Go, A. Maturana, T.S. Fisher, S.V. Garimella, Enhancement of external forced convection by ionic wind, Int. J. Heat Mass Transfer 51 (2008) 6047–6053.
[14] A.O. Ahmedou, M. Havet, Analysis of the EHD enhancement of heat transfer in a flat duct, IEEE Trans. Dielectr. Electr. Insul. 16 (2009) 489–494.
[15] M. Huang, F.C. Lai, Numerical study of EHD-enhanced water evaporation, J. Electrostat. 68 (2010) 364–370.
[16] C. Chaktranond, P. Ratanadecho, Analysis of heat and mass transfer enhancement in porous material subjected to electric fields (effects of particle sizes and layered arrangement), Exp. Therm. Fluid Sci. 34 (2010) 1049–1056.
[17] S. Saneewong Na Ayuttaya, C. Chaktranond, P. Rattanadecho, T. Kreewatcharin, Effect of ground arrangements on swirling flow in a channel subjected to electrohydrodynamic effects, ASME J. Fluids Eng. 134 (2012). pp. 051211-9.
[18] S. Saneewong Na Ayuttaya, C. Chaktranond, P. Rattanadecho, Numerical analysis of influence of electrode position on fluid flow in a 2-D rectangular duct flow, J. Mech. Sci. Technol. in press.
[19] M.V.D. Bonis, G. Ruocco, A generalized conjugate model for forced convection drying based on an evaporative kinetics, J. Food Eng. 89 (2008) 232–240.
[20] F. Marra, M.V.D. Bonis, G. Ruocco, Combined microwaves and convection heating: a conjugate approach, J. Food Eng. 97 (2010) 31–39.
[21] D.J. Griffiths, Introduction to Electrohydrodynamics, Prentice Hall International, Inc., New Jersey, 1999. p. 105.
[22] L.D. Landau, E.M. Lifshitz, Electrohydrodynamics of Continuous Media, Pergamon, New York, 1963.
[23] W. Klinbun, P. Rattanadecho, Numerical model of microwave driven convection in multilayer porous packed bed using a rectangular waveguide, ASME J. Heat Transfer 134 (2012). pp. 0426051-10.
[24] S. Sungsoontorn, P. Rattanadecho, W. Pakdee, One-dimensional model of heat and mass transports and pressure built up in unsaturated porous materials subjected to microwave energy, Drying Technol. 29 (2011) 189–204.